Delft University of Technology

Document Version
Final published version

Important note
To cite this publication, please use the final published version (if applicable).
Please check the document version above.

Corrosion protection of sintered nano-copper in chlorine-rich environments based on atmospheric pressure plasma jet surface treatment

Jinyuan Zhang [a], Wei Chen [a], Junwei Chen [a], Baotong Guo [a], Hongyu Tang [a], Chuan Chen [d], Guoqi Zhang [c], Jiajie Fan [a,b,c,*]

[a] Shanghai Engineering Technology Research Center of SiC Power Device, College of Intelligent Robotics and Advanced Manufacturing, Fudan University, Shanghai 200433, China
[b] Research Institute of Fudan University in Ningbo, Ningbo 315336, China
[c] EEMCS Faculty, Delft University of Technology, Delft 2628, the Netherlands
[d] State Key Laboratory of Environmental Adaptability for Industrial Products, China National Electric Apparatus Research Institute Co., Ltd, Guangzhou 510663, PR China

ABSTRACT

With the rapid development of new energy vehicles and offshore wind power systems in coastal cities, the application scale of power devices is constantly increasing. However, the corrosion problem of power packaging interconnection materials caused by the humid air and chlorine-rich environment near the sea is gradually emerging. This study addresses the corrosion protection of sintered nano-copper by innovatively employing atmospheric pressure plasma jet (APPJ) technology with hexamethyldisiloxane (HMDSO) as precursor to construct organic-inorganic hybrid hydrophobic coatings on copper surfaces. Experimental results demonstrate that the coating exhibits a three-dimensional crosslinked Si-O network structure. The synergistic effect between surface micron-scale spherical clusters and methyl groups elevates the contact angle by 50 % to 153.1° Electrochemical characterization reveals that the coating positively shifts corrosion potential by 0.035 V and reduces corrosion current density from 6.008×10^{-7} A/cm^2 to 5.542×10^{-7} A/cm^2, while maintaining higher activation energy across the experimental temperature range (30–60°C). EIS tests show that the coating effectively increases the charge transfer impedance of the sample, indicating an improvement in corrosion resistance. The 168-hour immersion test confirms effective barrier against Cl$^-$ corrosive attack with preserved substrate integrity. Density functional theory (DFT) simulations elucidate that unsaturated methylated fragments in HMDSO preferentially graft onto copper surface via chemisorption, where strong interfacial bonding energies (-2.26 ~ -4.38 eV) facilitate cleavage and crosslinking to form stable siloxane networks. This work proposes a novel anti-corrosion surface engineering strategy for copper interconnects, while revealing the plasma-induced interfacial bonding mechanisms of hybrid coatings, providing both theoretical and experimental foundations for developing durable electronic packaging materials.

1. Introduction

With the rapid development of the new energy sector, power electronic devices are being widely applied in new energy vehicles and offshore wind power, among other applications [1–3]. Advances in wide-bandgap (WBG) semiconductors have enhanced the performance of power electronic devices [4–6], but the resulting high power density and operating temperatures pose new challenges for packaging processes. In particular, the metal components in packaging structures are susceptible to corrosion from environmental pollutants, especially in

specific environments such as coastal areas or near fertilizer plants. Corrosive media like moisture, salts, and H₂S can significantly damage metal materials [7–9]. Copper (Cu), with its high melting point, excellent electrical conductivity, and mechanical properties, overcomes the migration failure issues of traditional lead-free solders under high-temperature and high-pressure conditions, making it widely used for the long-term stable operation of power devices [10–13]. In recent years, nanometal particle solder paste has attracted significant attention due to its ability to sinter at low temperatures into metals with excellent electrical conductivity, thermal conductivity, and high-temperature

resistance [14–15]. Among these, sintered Cu, with its lower cost and excellent performance, shows great potential as a high-temperature chip bonding material [16–18]. However, this trend also places higher demands on the reliability of chip packaging materials.

Currently, a significant amount of research has focused on the corrosion protection of sintered metal materials in harsh environments [19–20], such as the corrosion behavior of sintered Cu joints in humid H₂S environments and the migration phenomenon of sintered silver in electrolytes [21–22]. Hydrophobic treatments of metal surfaces have become an effective corrosion protection strategy, where low surface energy materials are roughened or low surface energy coatings are deposited to isolate corrosive substances [23–24]. Common methods for preparing superhydrophobic copper-based surfaces include electrodeposition [25], sol-gel processes [26–27], hydrothermal synthesis [28–29] and spraying [30–31]. Song et al [25] prepared a composite coating of nickel/myristate zinc (ZnMA) on Cu plates through electrodeposition technology. The coating exhibited superhydrophobicity and good corrosion resistance. Li et al [31] innovatively constructed a STA@TiO2/PU superhydrophobic coating on the surface of aluminum-lithium alloy through a low-cost spraying process. This coating exhibits excellent corrosion resistance, self-cleaning, anti-fouling, and anti-icing properties. However, these methods typically require immersing the entire sample in a reactor, posing challenges for applying them to metal components in packaging structures. In recent years, using the atmospheric pressure plasma jet (APPJ) for localized surface modification has become a feasible method. Silva et al [32] used hexamethyldisiloxane (HMDSO) monomer as the polymerization agent and deposited organosilicon films on the surface of SAE 1020 steel by using an APPJ system. They investigated the effects of different process parameters on the films and ultimately concluded that the three-step deposition method was more effective in improving corrosion resistance than continuous film deposition. Zhu et al [33] proposed a new treatment method based on plasma-assisted thin film deposition, which suppresses defects at the Cu/epoxy (EP) interface. By applying APPJ treatment, a silicon-containing film is deposited on the epoxy surface, significantly enhancing hydrophobicity, extending the creepage distance, and improving electrical insulation performance. Although there are already studies on the surface modification of metals using the APPJ process, its application in surface modification of interconnection metal structures is still rare. Moreover, there is still a lack of research on the film formation mechanism and corrosion protection mechanism of this process.

Density functional theory (DFT) calculations are often employed to analyze the interactions between coatings and substrates. Mahamdi et al [34] proposed a novel coating material, Alg-Ep-STO, for Cu corrosion prevention and analyzed the adsorption mechanism of this molecule on the Cu surface through DFT calculations. Ekeocha et al [35] combined DFT and molecular dynamics (MD) to deeply investigate the anti-corrosion ability of newly developed antipyrine derivatives for mild steel in an acidic environment. However, there are few studies on the film formation mechanism of plasma-assisted deposition on metal surfaces.

This study innovatively addresses the corrosion failure of sintered copper materials in harsh service environments by using APPJ technology to build silicon-based hydrophobic functional coatings on the surface, and the film formation mechanism of the APPJ process on Cu substrate is deeply analyzed through DFT simulations. Through systematic experimental characterization and theoretical calculations, it is revealed that the coating has a three-dimensional cross-linked silica network structure. The rough morphology formed by micron-sized particles on the surface, combined with the low surface energy of methyl groups, enhances hydrophobic performance by 50 %. The results of polarization curve and EIS curve tests show that the coating exhibits excellent corrosion protection performance and significant thermal stability advantages. Through 168-hour immersion test and DFT simulations, the study elucidates the grafting-crosslinking growth

mechanism, where the methylated fragments in the precursor HMDSO molecules dominate the chemical adsorption process. This strong interface interaction maintains the structural integrity and hydrophobicity of the coating under long-term corrosion conditions. The results provide not only a novel surface protection strategy for Cu interconnection materials in power modules but also theoretical and experimental foundations for developing long-lasting protective power electronic interconnection materials.

2. Materials and methodologies

2.1. Material preparation

In this work, we investigate the corrosion mechanisms and corrosion prevention strategies associated with sintered nano-Cu materials. The size of the sintered Cu samples utilized in this work is 5 × 5 × 1 mm. The sintered Cu paste contains Cu nanoparticles with an average particle size of 150–300 nm, with ethylene glycol (99.5 %, from Aladdin Reagent Co., Ltd.) and terpineol (95.0 %, from Aladdin Reagent Co., Ltd.) serving as solvents. As shown in Fig.1(a), after injecting the paste into the customized molds, they were firstly baked in a vacuum oven (DZF-6012, YIHENG) at 120 °C for 30 min to remove most of the solvents. Subsequently, the samples were pressure-sintered using a sintering machine (Sinterstar Innovate-F-XL, Boschman) under a nitrogen atmosphere at 250 °C, 20 MPa, for a duration of 25 min, resulting in bulk sintered Cu samples.

2.2. APPJ treatment

The schematic diagram of the APPJ system used for film deposition is shown in Fig. 1(b). The precursor hexamethyldisiloxane (HMDSO, Shanghai Aladdin Biochemical Technology Co., LTD.) is blown out by high purity argon through the bubbling method and then fully mixed in the mixing chamber before entering the reactor. After being ionized to form plasma under high voltage, it is blown out by the gas flow and finally grafts and crosslinks on the sample surface to form a hydrophobic coating. The working photo and structural schematic diagram of the reactor are shown in Fig. 1(c) and (d), respectively. The reactor contains a quartz tube as the reaction container and to limit the size of the jet, a Cu needle as the anode, and a Cu tape about 6 mm wide wound around the outside of the quartz tube as the ground electrode. The inner diameter of the quartz tube is 6 mm, the outer diameter is 8 mm, and the length is 140 mm. The distance between the bottom end of the Cu tape and the tail end of the tube opening, as well as the distance between the end of the Cu needle and the top end of the tape, is 15 mm. During operation, gas was blown into the top of the quartz tube. A breakdown discharge occured between the tip of the Cu needle electrode and the ground electrode, causing the HMDSO molecules in this space to ionize and generate plasma. Subsequently, it was blown out from the end of the quartz tube, forming a purple plasma plume.

The output voltage and repetition frequency affect the plume morphology and completeness of ionization reaction in reactor, while the distance between tube outlet and sample surface affects the deposition effect on the sample surface. In this work, the parameters for APPJ treatment are determined based on our preliminary adjustment as well as some previous studies [33]. In this work, the distance between the end of the reactor and the sample surface was maintained at approximately 20 mm to achieve optimal coating performance. The output voltage of the power supply was set to 10,000 V, the repetition frequency was 6 kHz, and the pulse width was 800 nanoseconds. The gas flow rate was regulated by a mass flow controller (Sevenstar D07–19), with the argon gas flow rate set at 1500mL/min and the HMDSO flow rate at 35mL/min. The APPJ film deposition process lasted a total of 12 min and was repeated four times for 3 min each deposition.
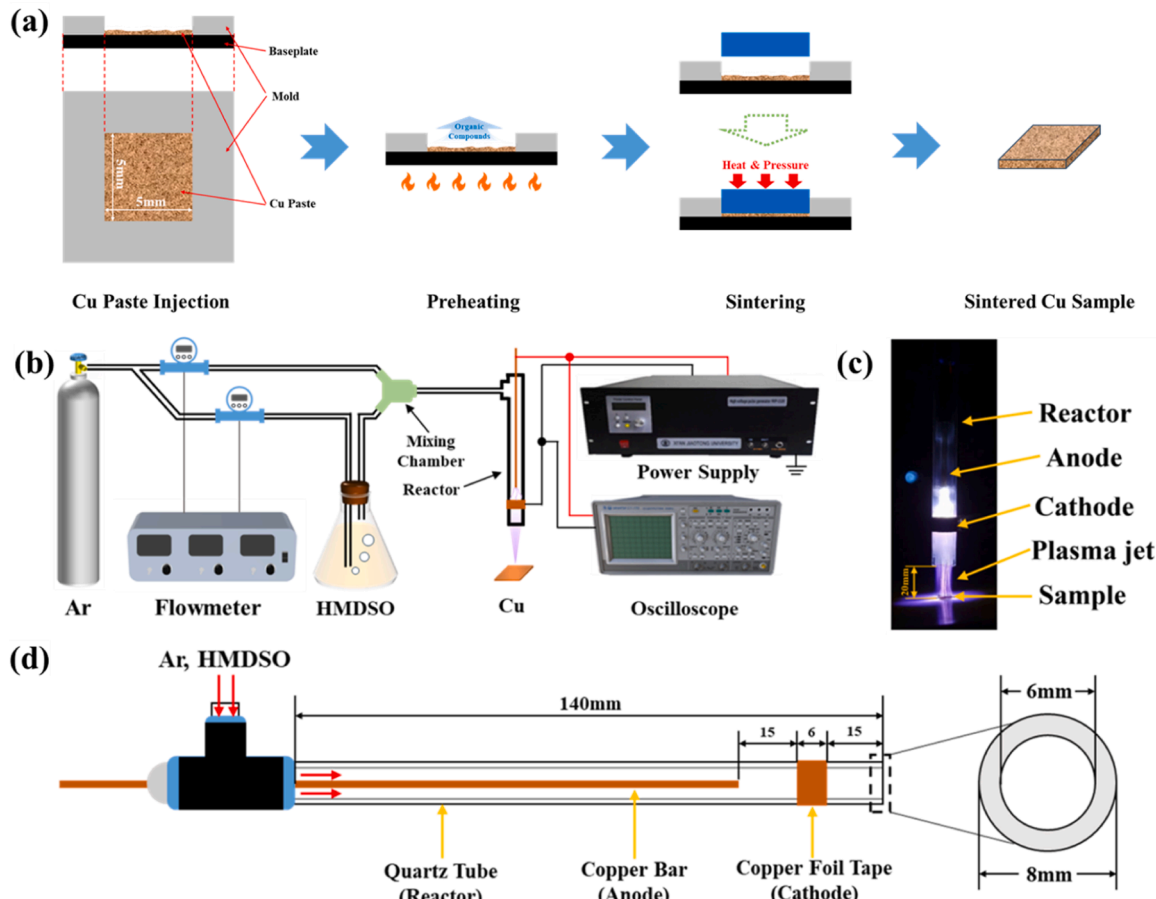
Fig. 1. (a) Schematic of the sintering process, (b) Setup of the APPJ treatment system, (c) photo of the reactor and (d) schematic diagram of the reactor structure.

2.3. Corrosion experiments

To evaluate the corrosion resistance of both coated and uncoated samples, electrochemical experiments and immersion corrosion tests were conducted. The electrochemical experiments were performed at room temperature and a series of preset temperatures (30 °C, 40 °C, 50 °C, 60 °C), using a typical three-electrode cell. The reference electrode was a saturated calomel electrode (SCE), the counter electrode was a platinum sheet electrode, and the sample under test served as the working electrode. The electrolyte used was a 3.5 % NaCl solution. The potentiodynamic polarization curves and electrochemical impedance spectroscopy (EIS) were measured using an electrochemical workstation (Chenhua CHI660e). In the polarization curve test, the scanning voltage range and scanning rate were set to $-0.15\sim0.5$ V and 5 mV/s respectively, while in the EIS test, the scanning frequency range and amplitude were set to $10^{-2}\sim10^5$ Hz and 15 mV respectively. For the immersion test, both types of samples were cleaned on their surfaces and then immersed in 3.5 % NaCl solution. The temperature of solution was controlled at 25 °C. After immersion for 168 h, the samples were taken out and cleaned before subjected to subsequent experiments.

2.4. Characterization methodology

Energy dispersive X-ray spectroscopy (SEM/EDS, Zeiss/GeminiSEM 360) was employed to analyze the surface morphology and elemental distribution of the samples. To determine the structure and composition of the samples, Fourier Transform Infrared Spectroscopy (FTIR, Thermo Nicolet IS50) and X-ray Photoelectron Spectroscopy (XPS, Shimadzu/ Axis Supra+) were utilized. To observe the coating thickness and corrosion depth, the samples were sectioned using a focused ion beam

(FIB/SEM, ZEISS Crossbeam 550) for subsequent observation and analysis. The XPS test results were processed with CasaXPS software.

3. Results and discusses

3.1. Characterization of coating samples

Fig. 2 (a-d) shows the surface morphology of the coated/uncoated samples. Compared with the relatively smooth surface of the untreated sintered Cu sample, the surface of the APPJ-treated sample is covered with many closely arranged cluster-like structures, with an average diameter of about 1 μm. Fig. 2(e) shows the cross-sectional details and EDS test results of APPJ-treated samples. Before FIB processing, both samples were treated with a gold spray of titanium. In the cross-sectional image of the coated sample, a dark and dense coating appears on the Cu surface, the cluster-like structures are closely cross-linked at the bottom. This structure can ensure a close connection between the coating and the sample surface while significantly enhancing the surface roughness of the sample. The average thickness of this coating is approximately 1.5 μm. The EDS scanning results show that the coating is mainly composed of Si and O elements.

The water contact angles of the sintered Cu samples before and after treatment were measured, and the measurement results are shown in Fig. 2(f) and (g). The average water contact angle of the untreated sample is 100.4°, while after APPJ deposition, the average water contact angle of the sample significantly increases to 153.1°, approximately 50 % higher than the samples before treatment. This is because the plasma deposition increases samples' surface roughness. When water droplets land on the surface, the cluster structures on the coating can trap air and form a stable air-liquid layer between the water and the sample surface,
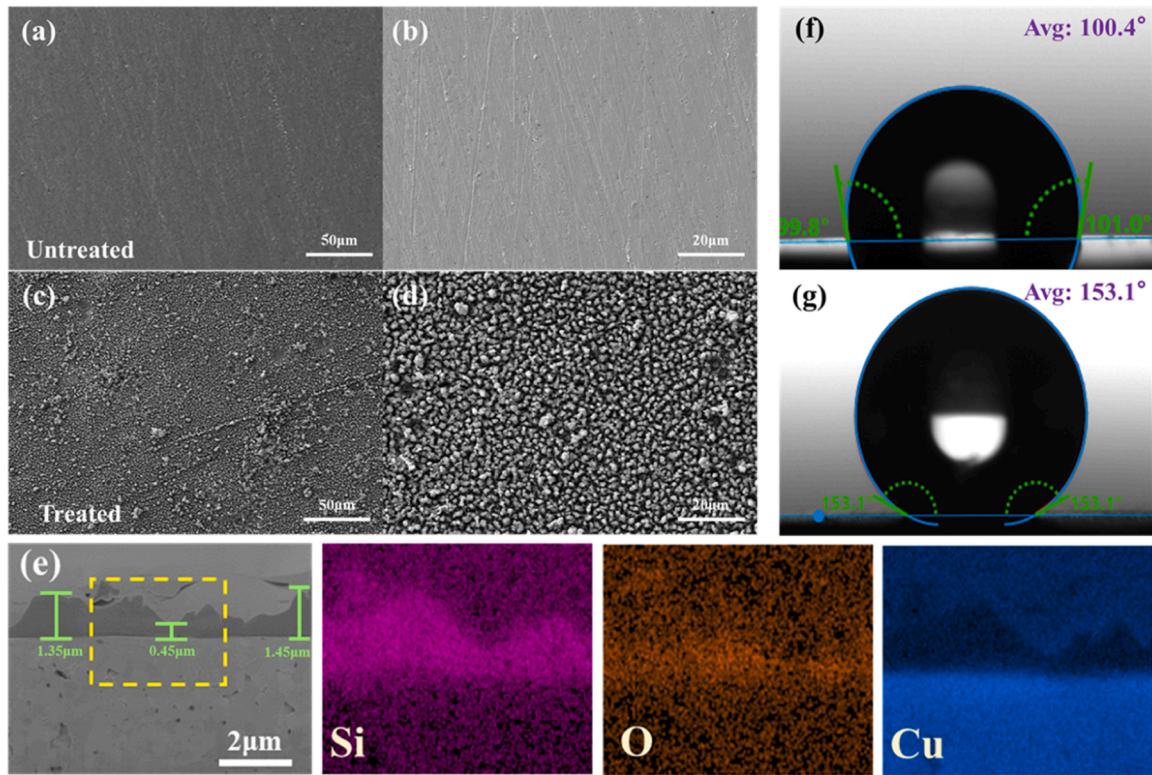
Fig. 2. Vertical-views SEM images of (a-b) untreated samples and (c-d) plasma treated samples, (e) section-view SEM image and EDS results of plasma treated sample, water contact angle images of (f) untreated sample and (g) plasma treated sample.

weakening the adhesion of water droplets.

The FTIR and XPS test results were used to further analyze the chemical configuration of the coating composition, as shown in Fig. 3(a-F). From the transmission spectrum, some characteristic peaks of silicon-containing functional groups can be found, including Si-O-Si, Si(CH$_3$)$_3$ and SiCH$_3$ [33]. The XPS wide-spectrum scan results reports the content of each element in the coating, with 28.71 % Si2p, 47.60 % O1s, and 23.69 % C1s. Additionally, we conducted narrow-spectrum scans of Si2p O1s, and C1s to analyze the chemical states of elements and characterize the molecular structure in the coating. For the Si2p peak, it contains 45.42 % of the SiO$_3$ peak (102.9 eV), 40.91 % of the SiO$_2$ peak (102.1 eV) and 22.81 % of the SiO$_4$ peak (103.9 eV); while in the O1s peak, it contains 75.75 % of the Si-O peak (532.7 eV) and 24.25 % of the C—O peak (533.6 eV); and the C1s peak contains 77.19 % of the C-Si peak (284.7 eV) and 22.81 % of the C—O peak (287.0 eV) [33,36]. The XPS results indicate that the Si and O elements in the coating mainly exist in the form of a Si-O network. After the decomposition of the precursor HMDSO, formed molecular fragments crosslink on the treated surface to form a film, and this crosslinked network contains a certain amount of methyl groups. In addition, the undetectable Cu2p peak indicates that the coating deposited on the Cu surface via APPJ has a good encapsulation effect.

3.2. Corrosion protection performance

In order to compare the corrosion susceptibility of sintered Cu samples before and after APPJ deposition, electrochemical experiments are conducted on both coated and uncoated samples. Fig. 4(a) presents the polarization curves of the two types of samples at room temperature. From the polarization curves, parameters such as corrosion potential (E$_{corr}$), corrosion current density (I$_{corr}$), and Tafel slopes for the cathodic and anodic regions are obtained, as shown in Table 1. After APPJ treatment, the coating positively shifts E$_{corr}$ by 0.035 V and reduces I$_{corr}$ from 6.008×10^{-7} A/cm^2 to 5.542×10^{-7} A/cm^2, indicating that the

coated samples have a lower corrosion tendency in NaCl solution. Additionally, to further analyze the effect of the silicon-containing hydrophobic coating on the corrosion susceptibility of the sintered Cu samples from a kinetic perspective, polarization curves are measured for both types of samples at a series of different temperatures (303, 313, 323 and 333 K), and the relationship between I$_{corr}$ and temperature is plotted in Fig. 4(b). The results indicate that within the experimental temperature range, the average I$_{corr}$ of both samples increase with rising temperature, and the I$_{corr}$ of the APPJ-deposited samples is consistently lower than that of the undeposited samples. The difference in corrosion current density between the two samples decreases with increasing temperature. Corrosion current density is positively correlated with corrosion current and corrosion rate, so the relationship between I$_{corr}$ and reaction temperature conforms to the Arrhenius equation [37]:

$$\ln k = -\frac{E_a}{RT} + \ln A \tag{1}$$

Eq. (1) represents the exponential form of the Arrhenius equation, where k is the reaction rate constant ($k \propto$ I$_{corr}$), E_a is the activation energy of the reaction, R is the molar gas constant, T is the temperature, and A is the pre-exponential factor. According to the Arrhenius equation, the obtained data are fitted to determine the activation energy of the corrosion reaction for both samples, as summarized in Table 1. The activation energy of the APPJ-coated samples is significantly higher than that of the uncoated samples, suggesting that the silicon-containing hydrophobic coating enhances the corrosion resistance of the sintered Cu.

Fig. 5(a) shows the Nyquist plots of the coated and uncoated samples and the corresponding fitting results. The corrosion resistance of the two samples in NaCl solution can be evaluated by the diameter of the impedance arc [31]. The results show that the impedance arc diameter of coated sample is larger than that of uncoated sample, indicating stronger corrosion resistance performance. Fig. 5(b-c) provides the Bode plots of the two samples. At the lowest frequency, the |Z| value of the
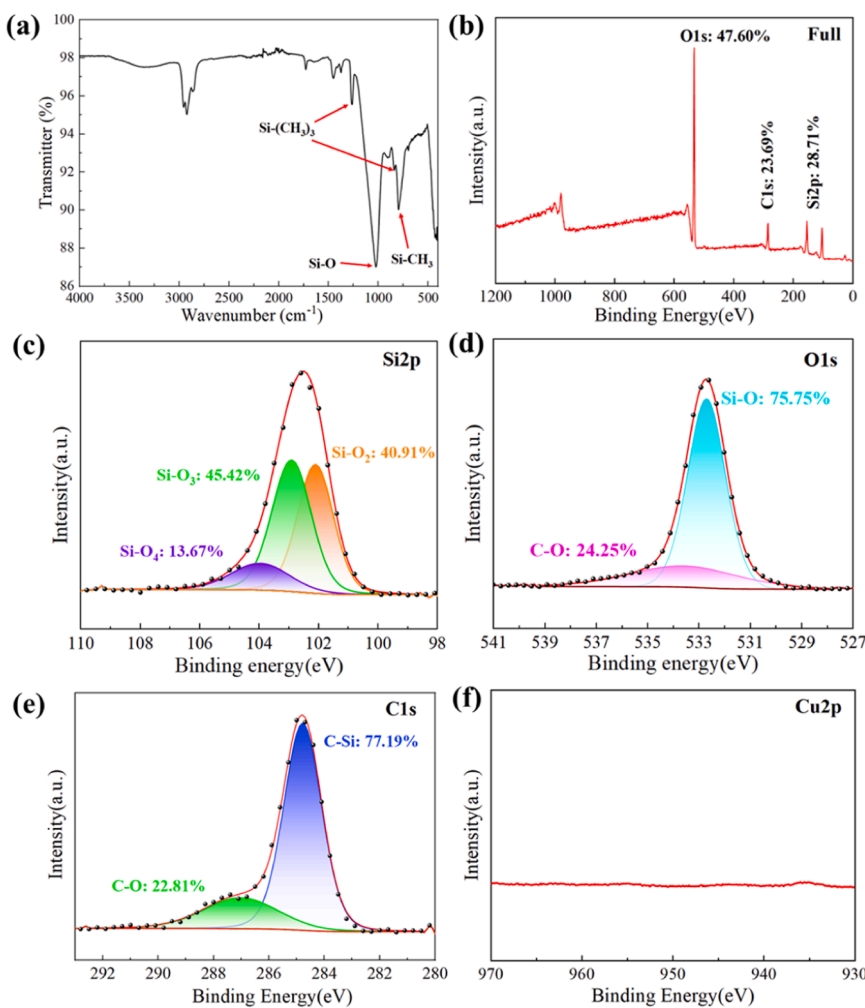
**Fig. 3.** (a) FTIR and (b-f) XPS spectra of coated samples.
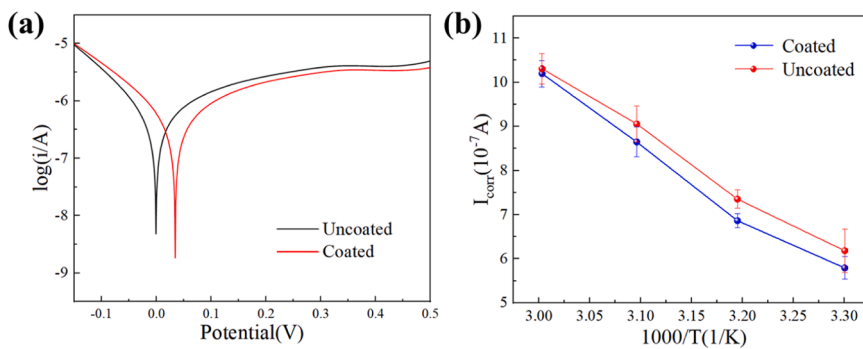
Fig. 4. (a) Polarization curves of two kinds of samples, (b) relationship between I_{corr} and temperature.

Table 1
Characteristic parameters obtained by polarization curves.

Sample	I_{corr} (10^{-7}A/ cm^2)	E_{corr} (V)	β_a (V/ dec)	β_c (V/ dec)	E_a (kJ·mol^{-1}·K^{-1})
Coated Sintered Cu	5.542	0.034	0.214	−0.133	16.157
Uncoated Sintered Cu	6.008	−0.001	0.222	−0.116	14.612

coated sample is approximately 2×10^4 $\Omega\cdot$cm^2, which is about 20 times of the uncoated sample, indicating that the deposited silicon-containing hydrophobic coating can effectively improve the corrosion resistance of the sample. Fig. 6 provides the chemical equivalent circuits of the two samples, and the corresponding parameters are listed in Table 2. In this model, R_s is the solution resistance, R_{ct} is the charge transfer resistance, and R_f is the resistance of the hydrophobic coating. CPE$_{dl}$ and CPE$_f$ refer to the double-layer capacitance and coating capacitance, respectively. The Warburg impedance W is observed in the coated sample, indicating the diffusion process of the electrolyte on the electrode surface. The results show that the R_{ct} of the coated sample is significantly higher than
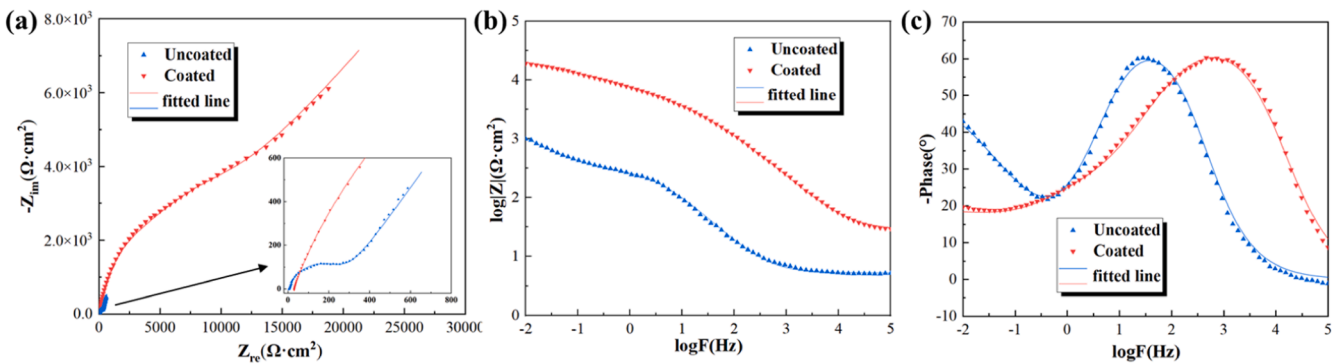
Fig. 5. EIS results of uncoated and coated samples: (a) Nyquist curve, (b) Bode |Z| versus frequency curve, (c) Bode phase angle versus frequency curve.
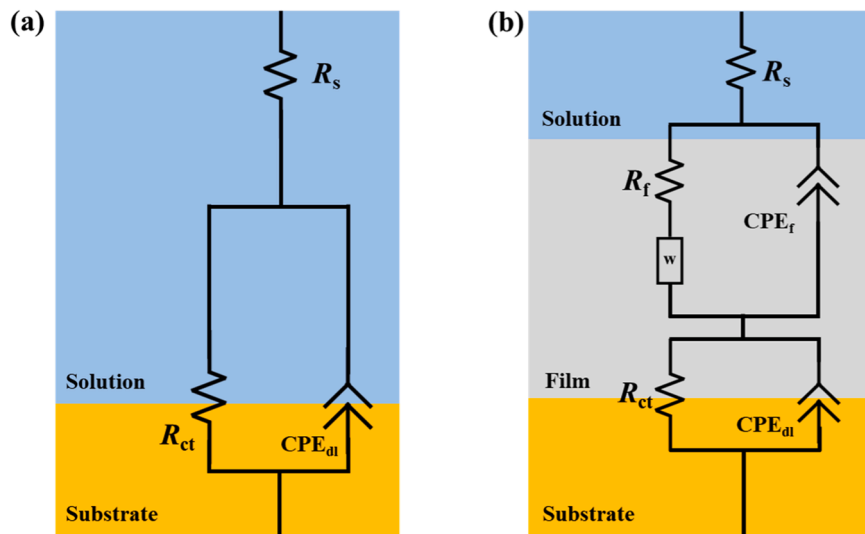

Fig. 6. Equivalent circuits for (a) uncoated sample and (b) coated sample.

Table 2
Fitting parameters of the equivalent circuits.

Samples	R_s ($\Omega \cdot cm^2$)	R_{ct} ($k\Omega \cdot cm^2$)	R_f ($k\Omega \cdot cm^2$)	CPE_{dl} ($\mu F \cdot cm^{-2}$)	CPE_f ($\mu F \cdot cm^{-2}$)	W ($\Omega \cdot cm^2$)
Uncoated	5.27	0.28	–	290.85	–	–
Coated	28.59	2.13	0.20	180.70	4.68	5048.8

that of the uncoated sample, indicating that the silicon-containing hydrophobic coating obtained in this study can provide corrosion protection for the sintered Cu sample in NaCl solution. The improvement in the corrosion resistance of sintered Cu in this study is less than that of APPJ coating on SAE 1020 steel in another study, which is related to the composition and size of the samples. Future research will focus on the optimization of APPJ processing technology and the influence of

substrate materials on coating performance.

Fig. 7 shows the surface optical micrographs of the coated and uncoated samples after 168 h immersion test. It can be clearly seen that the surface of the uncoated sample is severely corroded after immersion, with large corrosion spots; while the coating on the surface of the APPJ-processed sample remains intact, and no obvious corrosion marks are observed on the coated sample.
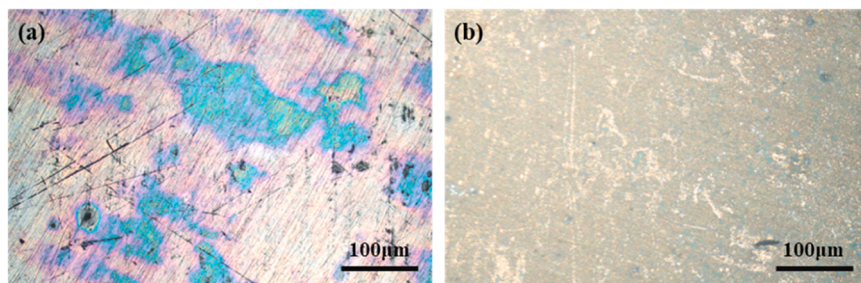

Fig. 7. Surface optical micrographs of (a) uncoated and (b) coated samples after immersion tests.

Fig. 8(a) and (c) present the surface and cross-sectional morphologies of the uncoated sample after immersion corrosion, the element distribution within the test area is illustrated as well. It can be seen that obvious corrosion pits have appeared on the surface of the sample. Some Cu particles detached due to corrosion and aging proceed in the solution, leading to further reactions in the internal structure and a tendency towards loosening and shedding. In the cross-sectional pattern, It can be clearly observed that a dark area diffusing inward has appeared at the top of the sample, with an average diffusion depth of approximately 1 μm. This area is consistent with the O element enrichment area in the EDS scanning results, and the overall content of Cl element is low without obvious enrichment, indicating that the corrosion products are mainly Cu oxides. Notably, in the oxide layer area, the tiny pore structure originally present in the sintered body shows a trend of volume expansion and lateral cracking, which will eventually lead to the detachment of the top sintered body, forming new corrosion pits and promoting further corrosion.

To analyze the specific composition of the corrosion products, XPS detection is conducted on the undeposited samples after corrosion, and the test results are shown in Fig. 9(a-c). The Cu 2p3/2 peak and 2p1/2 peak are located at 930.4 eV and 950.5 eV respectively. Among them, the Cu 2p3/2 peak shows two components, including the Cu^+ (Cu_2O) peak at 932.4 eV and the Cu^{2+} (CuO) peak at 934.4 eV; the Cu 2p3/2 peak is mainly produced by Cu^+ (Cu_2O); the satellite peaks of Cu_2O appear in the range of 940.1 eV to 946.2 eV. The O 1 s peak is mainly composed of 91.63 % C—O peak (from absorbed contaminants such as CO_2, etc.) and 8.37 % Cu_2O peak [38]. The XPS results indicate that Cu_2O is the main component of the corrosion products, and the content of CuO is relatively low. In addition, in the surface EDS scanning results, it was noted that there are point-like Cl element enrichment areas on the surface, indicating that a very small amount of Cu chloride was produced at individual points. In oxygen-containing neutral sodium chloride solution, the possible Cu chlorides that may form include CuCl and $Cu_2(OH)_3Cl$. The chemical reactions that occur during the corrosion process can be summarized as follows [39–41]:

In a neutral NaCl solution containing oxygen, Cu undergoes oxidation to form Cu^+;

$$Cu \rightarrow Cu^+ + e^- \tag{2}$$

subsequently, Cu^+ reacts with Cl^- ions in solution to produce CuCl and $CuCl_2^-$;

$$Cu^+ + Cl^- \rightarrow CuCl_{ads} \tag{3}$$

$$CuCl_{ads} + Cl^- \rightarrow CuCl_2^- \tag{4}$$
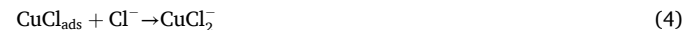
then, $CuCl_2^-$ precipitates to form a Cu_2O film;

$$2CuCl_2^- + H_2O \rightarrow Cu_2O + 2H^+ + 4Cl^- \tag{5}$$
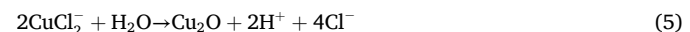
furthermore, some Cu_2O may react further to yield $Cu_2(OH)_3Cl$.

$$Cu_2O + Cl^- + OH^- + H_2O \rightarrow Cu_2(OH)_3Cl + 2e^- \tag{6}$$
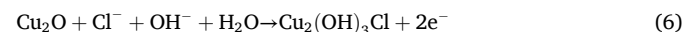
Fig. 8(b) and (d) exhibit the surface and cross-sectional morphology of the coated sample after immersion. From the surface morphology images of the samples, it can be observed that the spherical-cluster structure on the surface of the coating remains unchanged before and after immersion, and the integrity of the coating is not damaged. This indicates that the hydrophobic coating exhibits good physical stability in
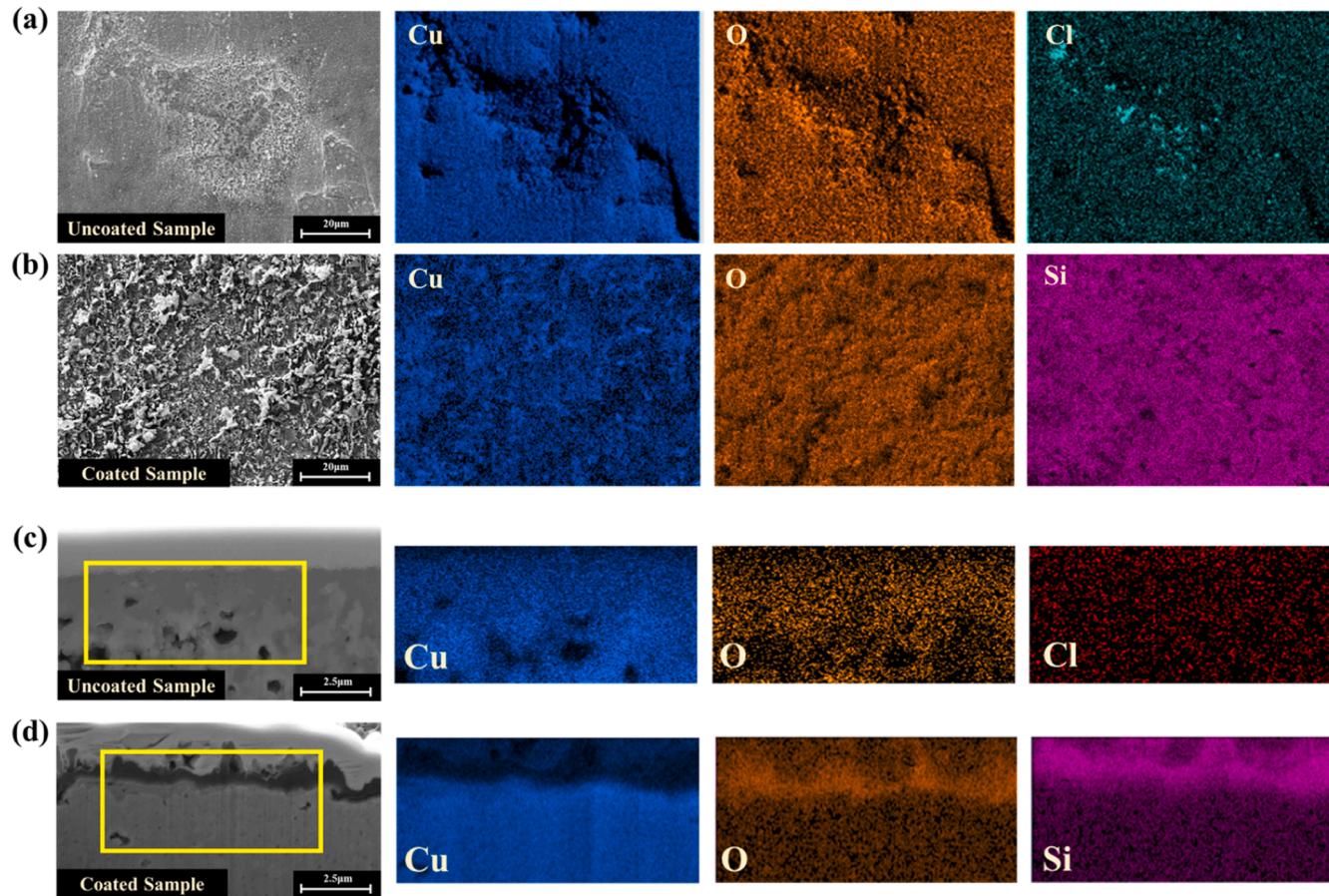
Fig. 8. The surface morphology of the (a) uncoated and (b) coated samples after immersion, and the cross-sectional morphology of the (c) uncoated and (d) coated samples after immersion.
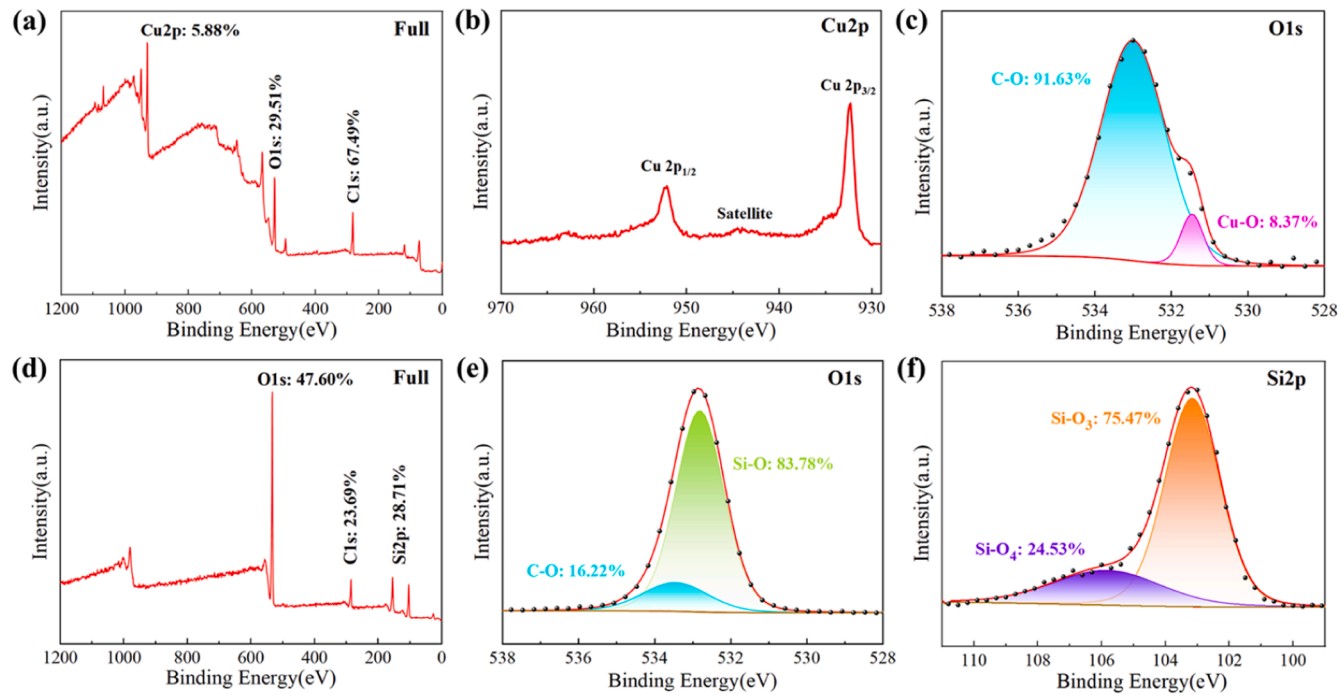
**Fig. 9.** XPS spectrum of the (a-c) uncoated and (d-f) coated samples after immersion.

the NaCl solution. Besides that, the photos of cross-sectional morphology indicates that the coating remains highly dense after immersion and is firmly bonded to the surface of the sintered Cu. No dark oxide layer is observed beneath the coating, and the pore size of the inner sintered Cu does not increase significantly. Moreover, the EDS results indicates that the O element is mainly concentrated in the coating area, and no enrichment of the O element is found in the interior of the sintered Cu. This proves that the Si-containing hydrophobic coating deposited by the APPJ process provides excellent corrosion protection for the sintered Cu samples.

Fig. 9(d-F) presents the XPS test results of the coated sample after immersion. In the full spectrum results, the Si2p, C1s and O1s peaks are observed at 102.3 eV, 285.4 eV and 533.4 eV respectively, with contents of 28.71 %, 23.69 % and 47.60 %. In the narrow spectrum scanning results, the Si2p peak contains two components, including 24.53 % of the SiO_4 peak (104.7 eV) and 75.47 % of the SiO_3 peak (102.7 eV), while the O1s peak is composed of 83.78 % of the Si-O peak (532.9 eV) and 16.22 % of the C—O peak (533.6 eV) [33,36]. This indicates that after immersion, the silicon-oxygen network structure in the coating remains intact and has not undergone a chemical reaction with the solution. The Cu2p peak shows almost no signal, suggesting that there is no damage to the coating surface and the barrier effect is good. The XPS results

demonstrate that this coating has good chemical stability in NaCl solution.

To verify the stability of the hydrophobic coating in NaCl solution, the water contact angle of the coated samples after immersion was tested. Fig. 10 presents the results of four measurements and the average value. The average water contact angle of the hydrophobic surface after 168 h of immersion is 147.70°, which has only decreased by 5.1° compared with the uncorroded samples. This indicates that the coating has good stability in NaCl solution and can maintain high hydrophobic performance for a long time.

Fig. 11 illustrates the corrosion protection mechanism of the silicon-containing hydrophobic coating. Without coating protection, in a humid atmosphere or immersion conditions, corrosive substances in water can directly contact and react with the Cu surface. However, for coated samples, the methyl groups in the Si-O network of the coating can reduce the surface energy, and the surface structure is rough, which not only effectively increases the water contact angle but also retains an air film within the coating under water droplet or immersion conditions, further preventing the direct contact of corrosive media with the substrate.
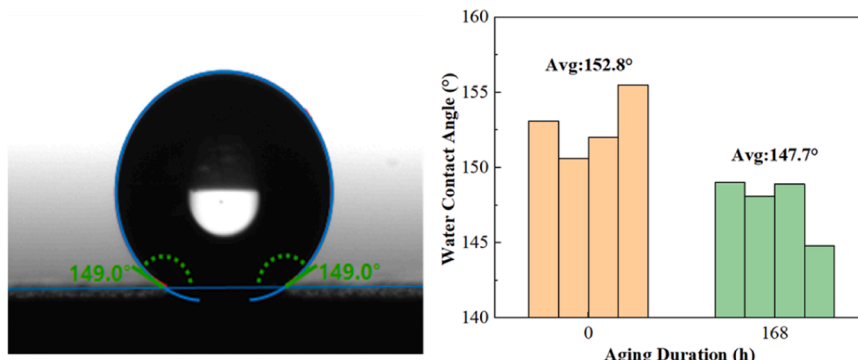

Fig. 10. The average water contact angle of coated samples before and after immersion.
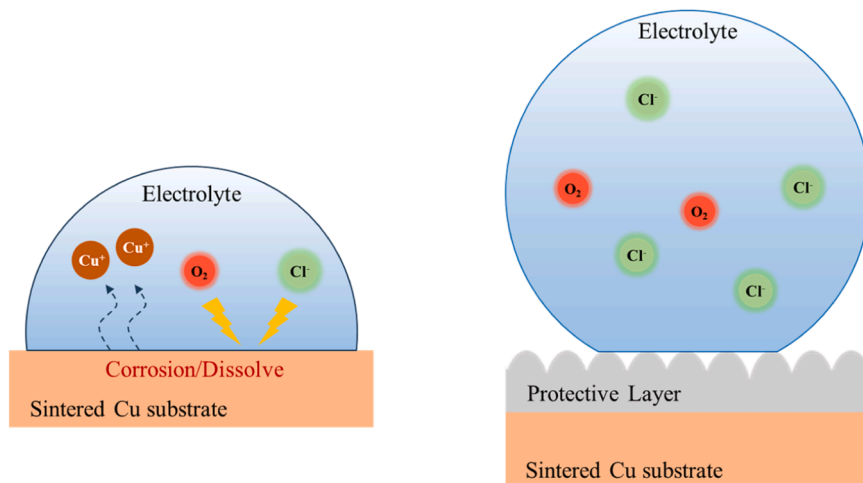
Fig. 11. Schematic diagram of the corrosion protection mechanism of silicon-containing hydrophobic coatings.

3.3. Theoretical study

3.3.1. Grafting mechanism of molecular fragments

In our APPJ process, the exited high energy electrons (e*) firstly motivate the gas molecules (Ar, O_2 and N_2) to form active particles (excited state Ar*, O_2*, N_2* and metastable state Ar_m) via collision ionization and Penning ionization. Then, the precursors–HMDSO molecules, will decompose into different molecular fragments under the impact of high-energy ions and deposit on sintered Cu surface driven by gas flow, as shown in Fig.12.

The equations of HMDSO cracking reaction are as follows [33]:

$$Ar_m + (CH_3)_3SiOSi(CH_3)_3 \rightarrow (CH_3)_3SiOSi^*(CH_3)_2 + CH_3 + Ar \qquad (7)$$

$$Ar^* + (CH_3)_3SiOSi(CH_3)_3 \rightarrow (CH_3)_3Si^* + (CH_3)_3SiO^* + Ar \qquad (8)$$
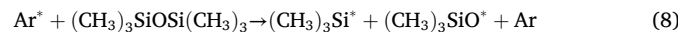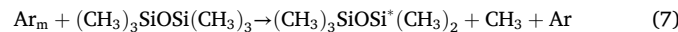
Some oxygen molecules will generate free oxygen atoms O* after ionization, local oxidation may occur in a short time before the molecular fragments deposit on Cu surface. Therefore, it is necessary to consider copper oxide when establishing the surface grafting model. Due to the short oxidation time, this study only considers the surface of Cu_2O which is preferentially generated.

In order to analyze the film formation mechanism on sintered Cu surface, the adsorption models of different molecular fragments are established through Density functional theory (DFT) calculations. The simulations are performed using Materials Studio software (Accelrys, Inc.). An energy path of dissociation of HMDSO molecules is illustrated in Fig. 13(a). The free energy of each dissociation step can be calculated through Eq. (9):

$$\Delta G_{reaction}^{298.15K} = \left(E_{ptotal} + G_{ptotal}\right) - \left(E_{rtotal} + G_{rtotal}\right) \qquad (9)$$

Where E_{ptotal} and G_{ptotal} represent the total electronic energy (E_{total}) and the zero-point corrected free energy (G_{total}) of the products, while E_{rtotal} and G_{rtotal} represent the above two energies of the reactants. The calculated E_{total} and G_{total} of all molecular fragments are shown in Table 3. Due to the cleavage of Si-O and Si-C bonds, the HMDSO molecule can be dissociated into $-OSi(CH_3)_3$, $-OSi(CH_3)_2$, $-OSiCH_3$, $-OSi$ with Gibbs free energy (ΔG) of each step are 103.4, 16.6, 67.6 and 14.3 kcal/mol. The ΔG values of all the steps are positive, thus the dissociation process cannot occur spontaneously and requires additional energy provided by plasma. And it can be observed that the first step is hardest with highest ΔG, while the generation of $-OSi(CH_3)_2$ and $-OSi$ fragments is relatively easy.

The Cu and Cu_2O (111) surfaces have exhibited lower surface free energy and higher stability in former studies [42,43], and are regarded as ideal models for surface adsorption research. Therefore, in this study, the (111) surfaces of Cu and Cu_2O are utilized for the theoretical studies. The Cu (111) surface is modeled with a 4-layer slab from a (3 × 2) supercell, while Cu_2O (111) surface is modeled with a 4-layer slab from
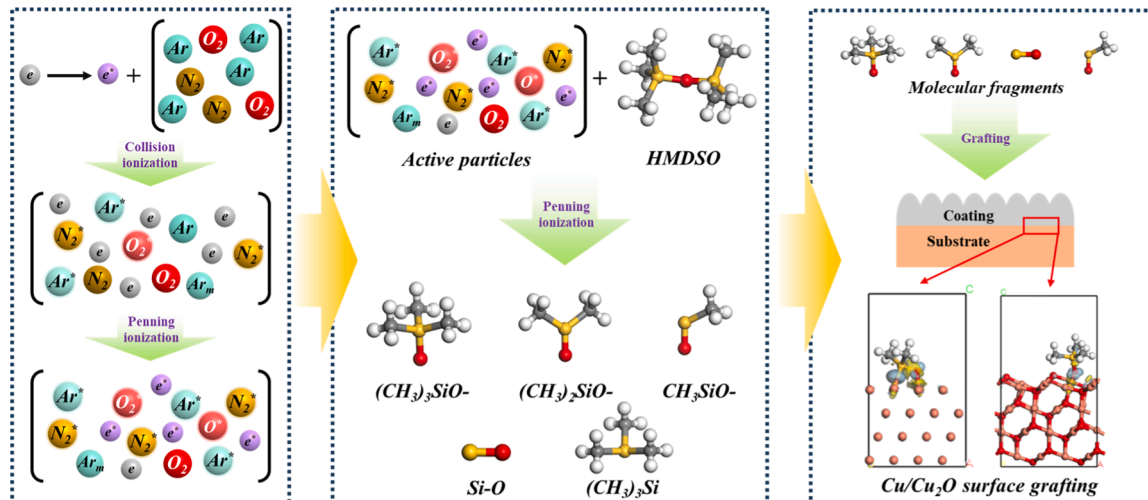

**Fig. 12.** Illustration demonstrating the APPJ coating process mechanism.
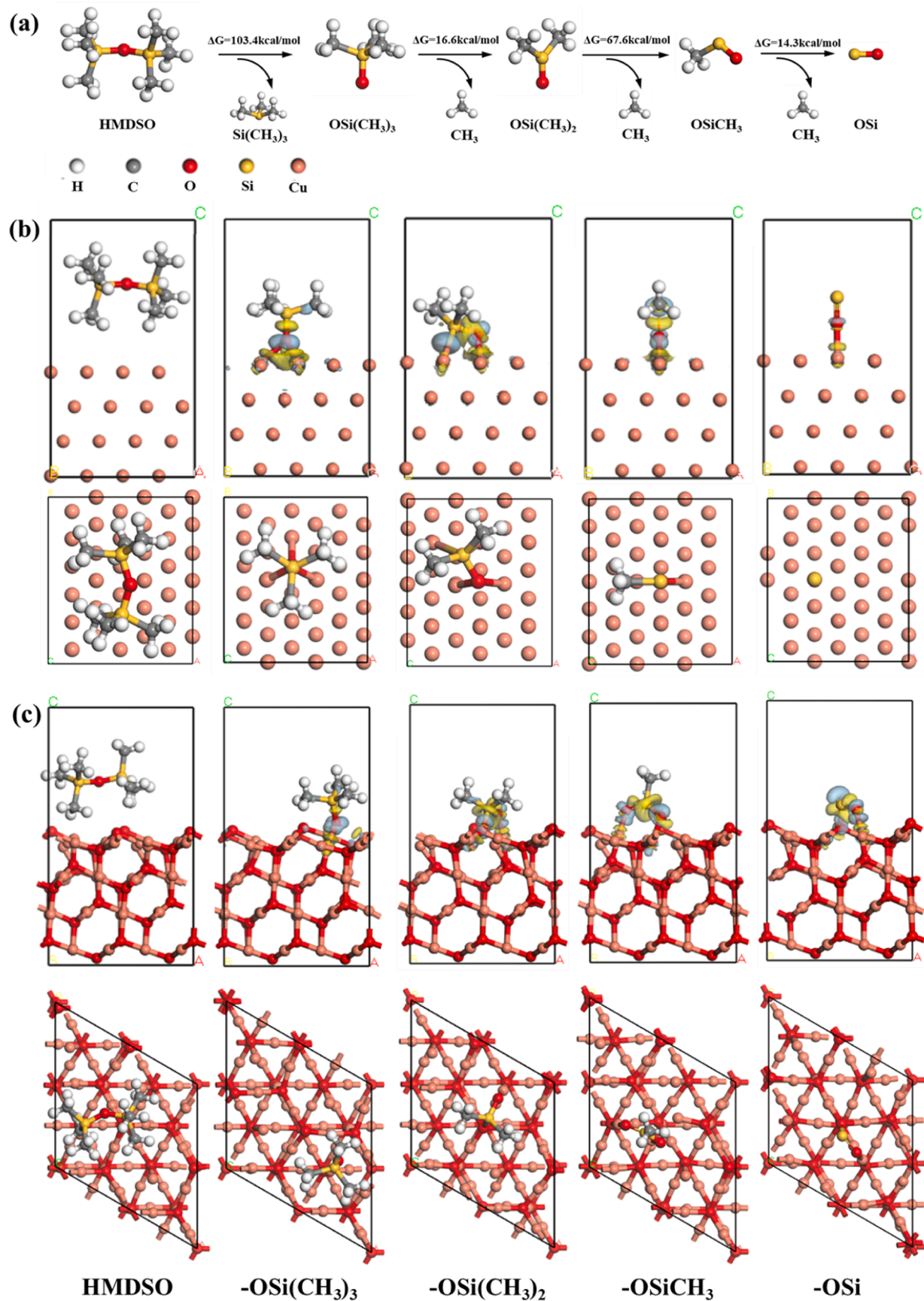
Fig. 13. (a)The molecular structure of HMDSO and its fragments; the adsorption models of different molecule fragments on (b) Cu surface and (c) Cu₂O surface.

Table 3
The calculated E_{total} and G_{total} of different molecular fragments.

Fragments	E_{total}(kcal/mol)	G_{total}(kcal/mol)
HMDSO	−560,870.565	110.440
$OSi(CH_3)_3$	−303,994.767	46.660
$OSi(CH_3)_2$	−278,982.347	28.752
$OSiCH_3$	−253,915.246	7.203
OSi	−228,904.514	−11.313
$Si(CH_3)_3$	−256,755.317	46.717
CH_3	−24,983.834	5.917

a (2 × 2) supercell. The generalized gradient approximation (GGA) method and Perdew-Burke-Ernzerhof (PBE) function are used to describe the exchange-correlation energy. The SCF tolerance, energy convergence tolerance, maximum force, and maximum displacement are set to 1E-5 eV·atom^{-1}, 2E-5 Ha, 0.004 Ha/Å and 0.005 Å, respectively. And a smearing value of 0.005 Ha is chosen to enhance SCF convergence. All DFT simulations (including the optimization of molecule/ion surface adsorption models and the analysis of film formation processes) were calculated by the DMoL^3 module with double numerical basis sets, including the polarization functions (DND) and basis file 3.5.

The optimized adsorption models of different fragments on Cu (111) and Cu$_2$O (111) are shown in Fig. 13(b) and (c), respectively. The charge density differences (CDD) are shown as well,in which the cyan areas indicate electron accumulation, and the yellow areas indicate electron depletion. The interaction energies between molecules/molecular fragments and Cu surface are utilized to evaluate the grafting strength and can be calculated through Eq. (10):

$$E_{inter} = E_{total} - (E_{sub} + E_{mol}) \tag{10}$$

Where E_{inter} refers to the interaction energy between molecular and Cu substrate, E_{sub}, E_{mol}, and E_{total} represent the total energies of Cu substrate, molecule and adsorption model, respectively. The more negative value of the interaction energy, the stronger the adsorption performance. The E_{inter} of different fragments on Cu and Cu$_2$O surface are shown in Table 4. In the Cu grafting model, the $OSi(CH_3)_3$ has the highest binding energy of −4.380 eV. With the decrease of methyl

Table 4
The interaction energy of different molecule fragments.

Structures	E_{total}(Ha)	E_{sub}(Ha)	E_{mol}(Ha)	E_{int}(Ha)	E_{int}(eV)
Cu(111)+ HMDSO	−105,879.920	−104,986.550	−893.369	−0.001	−0.028
Cu(111)+ OSi (CH$_3$)$_3$	−105,470.857	−104,986.542	−484.154	−0.161	−4.380
Cu(111)+ OSi (CH$_3$)$_2$	−105,430.943	−104,986.537	−444.284	−0.122	−3.337
Cu(111)+ OSiCH$_3$	−105,391.034	−104,986.568	−404.383	−0.083	−2.259
Cu(111)+ OSi	−105,351.128	−104,986.548	−364.555	−0.025	−0.680
Cu$_2$O (111)+ HMDSO	−108,107.103	−107,218.385	−888.716	−0.002	−0.054
Cu$_2$O (111)+ OSi (CH$_3$)$_3$	−107,700.206	−107,218.372	−481.680	−0.154	−4.190
Cu$_2$O (111)+ OSi (CH$_3$)$_2$	−107,660.720	−107,218.366	−442.158	−0.196	−5.333
Cu$_2$O (111)+ OSiCH$_3$	−107,621.139	−107,218.229	−402.737	−0.173	−4.707
Cu$_2$O (111)+ OSi	−107,756.517	−107,391.866	−364.546	−0.105	−2.857

groups, the interaction energies of other molecular fragments gradually decrease, but they are all higher than that of the HMDSO molecule. The unsaturated O atoms in the fragments serve as the principal participants in grafting process, and the stable adsorption sites of O atoms vary in different grafting models. Different adsorption sites lead to the variation in the number of chemical bonds that can be formed, eventually resulting in different interaction energies. The HMDSO molecule fails to form effective chemical adsorption with the Cu surface, therefore has a weaker interaction energy than other molecular fragments. While on the Cu$_2$O surface, due to the presence of unsaturated O adsorption sites, the unsaturated Si atoms in the molecular fragments can also form strong surface bonds. Therefore, the $OSi(CH_3)_2$, $OSiCH_3$, and OSi have higher interaction energy on Cu$_2$O surface.

1Ha=27.211eV

3.3.2. Analysis of the film growth process

Fig. 14 and 15 show the formation process of the hydrophobic film on Cu (111) and Cu$_2$O (111) surfaces, respectively. This process can be summarized into two steps: the grafting of methyl-containing molecular fragments $OSi(CH_3)_x$ onto the Cu/Cu$_2$O surface, and the cross-linking process among the grafted molecular fragments. In the Cu surface model, after the grafting is completed, some methyl groups are detached due to the impact of the plasma jet and are replaced by O atoms from the air. Subsequently, the unsaturated O and Si atoms bond with the nearby unsaturated sites, achieving the interconnection among the four grafted molecular fragments and forming a short Si-O chain. There are still unsaturated O and Si atoms in this Si-O chain, which can further form interconnections with nearby grafted fragments through a similar mechanism, eventually forming a large Si-O network covering the Cu surface. It should be noted that some discrete methyl groups can still modify the unsaturated O and Si atoms, forming -SiCH$_3$ and –OCH$_3$ structures, which helps to reduce surface energy and improve the hydrophobicity of the coating. The cross-linking film formation mechanism on the Cu$_2$O surface is similar. After the molecular fragments are grafted, they cross-link with the surrounding grafted fragments or the fragments deposited subsequently. Some unsaturated Si atoms within the siloxane network can be modified by free methyl groups, as shown in Fig. 15. Here, to simplify the model and make the image clear, the lower layers of the Cu$_2$O model are hidden, and Si-O fragments are used as all of the initial grafted molecular fragments.

3.3.3. Hydrophobic and anti-corrosion properties of the coating

The adsorption of H$_2$O molecules and Cl$^-$ on coated and bare Cu surfaces was used to evaluate the hydrophobic and corrosion protection properties of the coating. In the initial adsorption models, a small silicon-oxygen crosslinking layer was constructed on the top of the Cu layer and served as the hydrophobic processed model after optimization. The H$_2$O molecules and Cl$^-$ ions are placed 2.5 Å above the C atom in -CH$_3$ group and the Cu atom at the center of the surface, respectively. The geometry optimization results are shown in Fig. 16, and the interaction energy and adsorption distances are listed in Table 5. For the H$_2$O adsorption models, the adsorption distance increases both in coated and uncoated models, while the interaction energy of H$_2$O molecules in coated model is smaller, demonstrating stronger hydrophobic performance than bare Cu. In Cl$^-$ ion adsorption models, the bare Cu surface exhibits stronger adsorption intention towards the Cl$^-$, resulting in decreased adsorption distance and an adsorption energy of −3.477 eV, which is sufficient to form chemical adsorption. However, the coated model shows a lower E_{int} of −1.041 eV and increased adsorption distance, indicating that the hydrophobic coating can weaken the adsorption effect of Cl$^-$ ions on Cu surface and reduce the risk of corrosion.

4. Conclusions

In this study, we proposed a novel corrosion protection method for sintered Cu based on plasma-assisted deposition with HMDSO as the
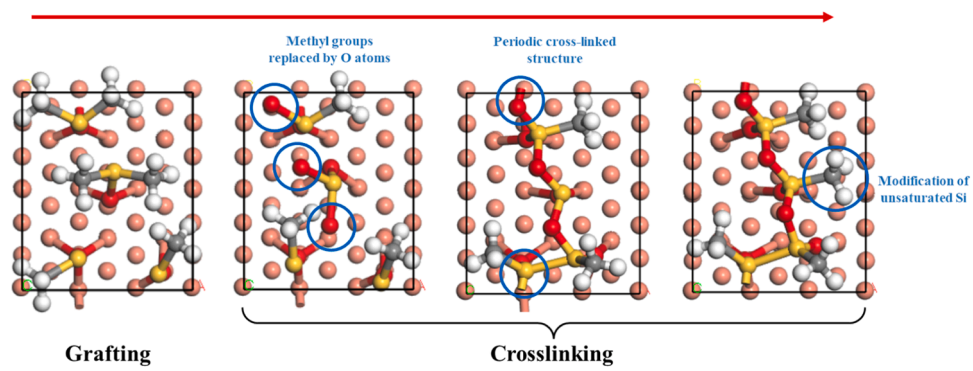
**Fig. 14.** The formation process of hydrophobic film on Cu (1 1 1) surface.
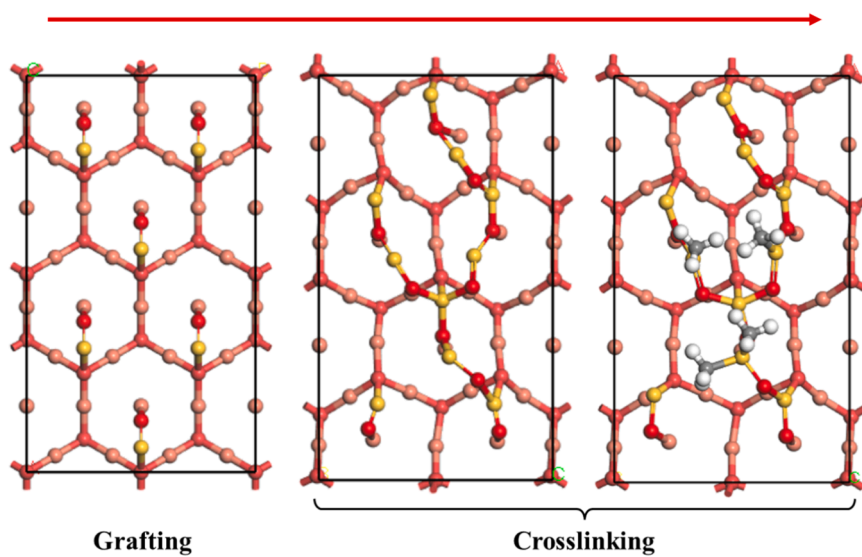
Fig. 15. The formation process of hydrophobic film on Cu_2O (1 1 1) surface.
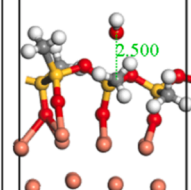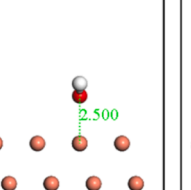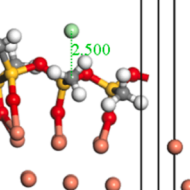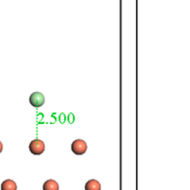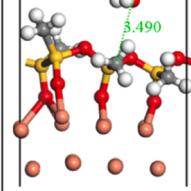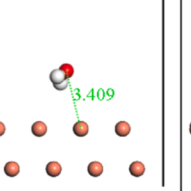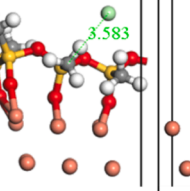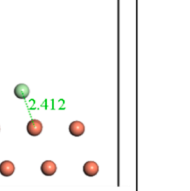
Fig. 16. The adsorption model of H_2O and Cl^- on hydrophobic layer and bare Cu surface.

Table 5

The E_{int} values and adsorption distances of different models.

Models	E_{int}(eV)	d_{abs}(Å)
H$_2$O on hydrophobic layer	−0.069	3.490
H$_2$O on Cu(111)	−0.097	3.409
Cl$^-$ on hydrophobic layer	−3.477	3.583
Cl$^-$ on Cu(111)	−1.041	2.412

precursor. A stable cross-linked organosilicon film with high hydrophobicity was deposited on the surface of sintered Cu samples. The microstructure, chemical composition and water contact angle of the film were characterized, and the corrosion protection performance of the coating in a chlorine-rich environment (3.5 % NaCl solution) was examined. DFT calculations were used to explain the film formation and hydrophobic mechanism. The main conclusions are summarized as follows:

(1) The coating was formed by numerous closely combined cluster-like particles at the micrometer scale, with the main component being a methyl-containing crosslinked siloxane network. The methyl groups' low surface energy and increased surface roughness significantly enhance the hydrophobicity of the samples by approximately 50 %.

(2) The coated samples exhibited excellent corrosion resistance in 3.5 % NaCl solution. The polarization curve and EIS test results indicated that, compared with the uncoated sample, the corrosion potential of coated sample shifted positively by 0.035 V, and it showed a lower corrosion current density and a higher reaction activation energy within the experimental temperature range (30℃−60℃). The |Z| value at the lowest frequency and charge transfer resistance R_{ct} of the coated sample were significantly higher than those of the uncoated sample. After 168 h of immersion corrosion test, the physical structure of the coating remained intact and the chemical composition was stable, with the contact angle decreasing by only 5.1°, and no obvious corrosion occurred on the bottom sintered Cu sample.

(3) The growth process of the film on Cu/Cu$_2$O surface is mainly divided into two stages: the grafting stage and the interconnection stage. The methyl-contained OSi(CH$_3$)$_x$ fragments, due to its easier grafting, becomes the main participant. After the group substitution of grafted molecules and intermolecular cross-linking, a silicon-oxygen network is formed. Some unsaturated O atoms and Si atoms are modified by discrete methyl groups, forming -SiCH$_3$ and –OCH$_3$ structures, which can improve the hydrophobicity of the coating.

This study presents a new method - atmospheric pressure plasma jet process - for surface corrosion protection of precision interconnection structures in power device packaging, successfully enhanced the corrosion resistance of sintered Cu in a chlorine-rich environment and conducted an in-depth analysis of the film formation mechanism on Cu/Cu$_2$O surface. Providing a new direction and theoretical basis for high-reliability power packaging.

CRediT authorship contribution statement

Jinyuan Zhang: Writing – original draft, Data curation, Conceptualization. **Wei Chen:** Writing – review & editing, Investigation, Formal analysis. **Junwei Chen:** Writing – review & editing. **Baotong Guo:** Writing – review & editing. **Hongyu Tang:** Writing – review & editing. **Chuan Chen:** Project administration, Funding acquisition. **Guoqi Zhang:** Supervision. **Jiajie Fan:** Writing – review & editing, Supervision, Resources, Project administration, Funding acquisition.

Declaration of competing interest

The authors declare that they have no known competing financial interests or personal relationships that could have appeared to influence the work reported in this paper.

Data availability

Data will be made available on request.

References

[1] K. Trapani, D.L. Millar, H.C.M. Smith, Novel offshore application of photovoltaics in comparison to conventional marine renewable energy technologies, Renew. Energ. 50 (2013) 879–888, https://doi.org/10.1016/j.renene.2012.08.043.

[2] S.K. Bhogaraju, H.R. Kotadia, F. Conti, A. Mauser, T. Rubenbauer, R. Bruetting, M. Schneider-Ramelow, G. Elger, Die-attach bonding with etched micro brass metal pigment flakes for high-power electronics packaging, ACS Appl. Electron. Mater. 3 (10) (2021) 4587–4603, https://doi.org/10.1021/acsaelm.1c00721.

[3] L. Feng, H. Shen, Y. Zhu, H. Gao, X. Yao, Insight into generation and evolution of sea-salt aerosols from field measurements in diversified marine and coastal atmospheres, Sci. Rep. 7 (2017) 41260, https://doi.org/10.1038/srep41260.

[4] H. Lee, V. Smet, R. Tummala, A review of SiC Power module packaging technologies: challenges, advances, and emerging issues, IEEE Trans. Emerg. Sel. Topics Power Electron. 8 (1) (2020) 239–255, https://doi.org/10.1109/JESTPE.2019.2951801.

[5] X. Wang, H. Wen, Y. Zhu, Review of SiC Power Devices for Electrical Power Systems: characteristics, Protection, and application, 2021 6th Asia Conference on Power and Electrical Engineering (ACPEE). (2021) 1–5. doi: 10.1109/ACPEE 51499.2021.9437108.

[6] A. Kar, K. Kundu, H. Chattopadhyay, R. Banerjee, White light emission of wide-bandgap silicon carbide: a review, J. Am. Ceram. Soc. 105 (5) (2022) 3100–3115, https://doi.org/10.1111/jace.18359.

[7] J. Chen, Y. Gong, Z. Yang, Failure analysis on the pin fin heat sink for the power module of new energy vehicles, Eng. Fail. Anal. 143 (2023) 106870, https://doi.org/10.1016/j.engfailanal.2022.106870.

[8] C. Qi, Z. Li, H. Bi, K.D. Johansen, Towards sustainable steel corrosion protection: expanding the applicability of natural hydrolyzable tannin in epoxy coatings via metal complexation, Electrochim. Acta. 497 (2024) 144546, https://doi.org/10.1016/j.electacta.2024.144546.

[9] J. Huo, B. Gao, B. He, W. Li, Y. He, J. Wang, Experimental, DFT, and MD calculation study on chain amino acids promoting uniform corrosion for copper surface planarization, Electrochim. Acta. 520 (2025) 145873, https://doi.org/10.1016/j.electacta.2025.145873.

[10] Y. Qian, F. Hou, J. Fan, Q. Lv, X. Fan, G. Zhang, Design of a fan-out panel-level SiC MOSFET power module using ant colony optimization-back propagation neural network, IEEE Trans. Electron Devices. 68 (7) (2021) 3460–3467, https://doi.org/10.1109/TED.2021.3077209.

[11] W. Chen, J. Jiang, A.H. Meda, M.S. Ibrahim, G. Zhang, J. Fan, A thin and low-inductance 1200 V SiC MOSFET fan-out panel-level packaging with thermal cycling reliability evaluation, IEEE Trans. Electron Devices. 70 (5) (2023) 2268–2275, https://doi.org/10.1109/TED.2023.3263150.

[12] L. Wang, T. Zhang, F. Yang, D. Ma, C. Zhao, Y. Pei, Y. Gan, Cu clip-bonding method with optimized source inductance for current balancing in multichip SiC MOSFET power module, IEEE Trans. Power Electron. 37 (7) (2022) 7952–7964, https://doi.org/10.1109/TPEL.2022.3141373.

[13] Z. Huang, Y. Li, L. Chen, Y. Tan, C. Chen, Y. Kang, F. Luo, A novel low inductive 3D SiC power module based on hybrid packaging and integration method, IEEE Energy Conversion Congress Exposition (ECCE) (2017) 3995–4002, https://doi.org/10.1109/ECCE.2017.8096698.

[14] X. Wei, X. Zhao, X. Tang, L. Wang, H. Zhang, Y. Tian, R. Han, Achievement and assessment of 6-in wafer bonding based on a novel nanosilver sintering method, IEEE Trans. Comp., Packag., Manufact. Technol. 15 (5) (2025) 1126–1134, https://doi.org/10.1109/TCPMT.2025.3541627.

[15] H. Li, A study on the failure evolution to short circuit of nanosilver sintered press-pack IGBT, IEEE Trans. Compon., Packag., Manuf. Technol. 10 (1) (2020) 184–187, https://doi.org/10.1109/TCPMT.2019.2957759.

[16] H. Lyu, C. Wang, K. Li, X. Jia, J. He, D. Yan, N. Lin, J. Duan, Sintering and optimization of copper nanopaste-connected copper array conical microstructures, Mater. Sci. Semicond. Process. 186 (2025) 109081, https://doi.org/10.1016/j.mssp.2024.109081.

[17] Y. Gao, W. Li, C. Chen, H. Zhang, J. Jiu, C. Li, S. Nagao, K. Suganuma, Novel copper particle paste with self-reduction and self-protection characteristics for die attachment of power semiconductor under a nitrogen atmosphere, Mater. Des. 160 (15) (2018) 1265–1272, https://doi.org/10.1016/j.matdes.2018.11.003.

[18] T.F. Chen, K.S. Siow, Comparing the mechanical and thermal-electrical properties of sintered copper (Cu) and sintered silver (Ag) joints, J. Alloys Compounds. 866 (2021) 158783, https://doi.org/10.1016/j.jallcom.2021.158783.

[19] X. Wang, Z. Yang, B. Wang, W. Chen, G. Zhang, J. Zhang, J. Fan, P. Liu, Effect of epoxy resin addition on properties and corrosion behavior of sintered joints in

power modules serviced offshore, J. Mater. Res. Technol. 25 (2023) 6593–6612, https://doi.org/10.1016/j.jmrt.2023.07.098.

[20] K. Jung, K. Min, C. Lee, B. Park, H. Jeong, J. Koo, B. Lee, S. Jung, Effect of epoxy content in Ag nanoparticle paste on the bonding strength of MLCC packages, Appl. Surf. Sci. 495 (2019) 143487, https://doi.org/10.1016/j.apsusc.2019.07.229.

[21] W. Chen, X. Liu, D. Hu, X. Liu, X. Fan, G. Zhang, J. Fan, Unraveling the hydrogen sulfide aging mechanism on electrical-thermal–mechanical property degradation of sintered nanocopper interconnects used in power electronics packaging, Mater. Des. 238 (2024) 112702, https://doi.org/10.1016/j.matdes.2024.112702.

[22] Y. Xu, Y. Liu, Z. Pan, K. Li, J. Lu, Q. Sun, Evaluating electrochemical migration behavior of sintered nano-Ag: factors of bias voltage, electrode spacing, sinter process parameters, and NaCl concentration, J Mater Sci: Mater Electron 34 (2023) 1971, https://doi.org/10.1007/s10854-023-11369-8.

[23] W. Sun, N. Wang, J. Li, S. Xu, L. Song, Y. Liu, D. Wang, Humidity-resistant triboelectric nanogenerator and its applications in wind energy harvesting and self-powered cathodic protection, Electrochim. Acta. 391 (2021) 138994, https://doi.org/10.1016/j.electacta.2021.138994.

[24] X. Chen, P. Wang, D. Zhang, J. Ou, Rational fabrication of superhydrophobic surfaces with coalescence-induced droplet jumping behavior for atmospheric corrosion protection, Chem. Eng. J. 428 (2022) 132029, https://doi.org/10.1016/j.cej.2021.132029.

[25] Z. Song, S. Zhang, L. Ding, T. Yao, Electrodeposited Ni/zinc myristate composite coating with long-time corrosion resistance, Corros. Eng. Sci. Technol. 60 (2025) 323–336, https://doi.org/10.1177/1478422X251337561.

[26] R. Figueroa, X.R. Nóvoa, C. Pérez, Hydrophobic surface treatments for improving the corrosion resistance of anodized AA2024-T3 alloys, Electrochim. Acta. 303 (2019) 56–66, https://doi.org/10.1016/j.electacta.2019.02.034.

[27] Y. Chen, Y. Liu, Y. Xie, H. Zhang, X. Du, Z. Zhang, Preparation of hydrophobic silane/graphene oxide composite coating implanted with benzotriazole to improve the anti-corrosion performance of copper, J. Alloys Compd. 893 (2022) 162305, https://doi.org/10.1016/j.jallcom.2021.162305.

[28] Y. Wan, M. Chen, W. Liu, X. Shen, Y. Min, Q. Xu, The research on preparation of superhydrophobic surfaces of pure copper by hydrothermal method and its corrosion resistance, Electrochim. Acta. 270 (2018) 310–318, https://doi.org/10.1016/j.electacta.2018.03.060.

[29] B. Wang, H. Pan, X. Lu, L. He, H. Zhang, X. Li, H. Guo, D. Zhou, Q. Xia, Copper-organic framework-derived porous nanorods for chemoselective hydrogenation of quinoline compounds at an aqueous/oil interface, ACS Appl. Nano. Mater. 4 (2021) 11779–11790, https://doi.org/10.1021/acsanm.1c02369.

[30] H. Yang, Y. Dong, X. Li, Y. Gao, W. He, Y. Liu, X. Mu, Y. Zhao, Anti-corrosion superhydrophobic micro-TiB2/nano-SiO2 based coating with "multi-scale hard particles-embedding-soft membrane" structure fabricated by spray deposition, Ind. Eng. Chem. 144 (2025) 496–511, https://doi.org/10.1016/j.jiec.2024.09.050.

[31] X. Li, C. Ma, T. Shi, H. Yang, Robust, fluorine-free, bioinspired PU superhydrophobic composite coating based on modified ceramics nanoparticle:

preparation, characterization and mechanism, Prog. Org. Coat. 204 (2025) 109226, https://doi.org/10.1016/j.porgcoat.2025.109226.

[32] L.L.G. Silva, F.V.P. Kodaira, P.V.M. Fagundes, A. Quade, K.G. Kostov, Study of organosilicon films deposited on SAE 1020 steel by atmospheric plasma jet for corrosion protection, Braz. J. Phys. 52 (2022) 114, https://doi.org/10.1007/s13538-022-01123-6.

[33] X. Zhu, X. Guan, L. Dai, X. Cui, J. Fan, Z. Fang, Improvement of electrical insulating properties for defective metal/epoxy resin interface in power modules by micro-plasma jet, Appl. Surf. Sci. 638 (2023) 158064, https://doi.org/10.1016/j.apsusc.2023.158064.

[34] M.E. Mahamdi, W. Daoudi, O. Dagdag, H.S. Kim, F. Eddaoudy, D.K. Verma, S. Gupta, A. Berisha, M. Loutou, B. Noureddine, A.E. Aatiaoui, Integrating experimental and theoretical studies in the development of a novel alginate-based bio-composite for copper anticorrosion in 3.5 % NaCl environments, Int. J. Biol. Macromol. 257 (2024) 128600, https://doi.org/10.1016/j.ijbiomac.2023.128600.

[35] C.I. Ekeocha, I.N. Uzochukwu, I.B. Onyeachu, I.N. Etim, E.E. Oguzie, Theoretical study of novel antipyrine derivatives as promising corrosion inhibitors for mild steel in an acidic environment, Struct. Chem. 36 (2025) 363–379, https://doi.org/10.1007/s11224-024-02368-4.

[36] D.S. Wavhal, J. Zhang, M.L. Steen, E.R. Fisher, Investigation of gas phase species and deposition of SiO2 films from HMDSO/O2 plasmas, Plasma Processes Polym.. 3 (3) (2006) 276–287. doi: https://doi.org/10.1002/ppap.200500140.

[37] J. Crapse, N. Pappireddi, M. Gupta, S.Y. Shvartsman, E. Wieschaus, M. Wuhr, Evaluating the Arrhenius equation for developmental processes, Mol. Syst. Biol. 17 (2021) e9895, https://doi.org/10.15252/msb.20209895.

[38] J.A.T. Ochoa, D.C. German, O.C. Martinez, M.B. Sanchez, G.G. Sosa, A.H. Gomez, Peak-fitting of Cu 2p photoemission spectra in Cu^0, Cu^{1+}, and Cu^{2+} oxides: a method for discriminating Cu^0 from Cu^{1+}, Appl. Surf. Sci. 622 (2023) 156960 https://doi.org/10.1016/j.apsusc.2023.156960.

[39] J. Xin, L. Fan, Y. Liu, L. Ma, Research progress on the corrosion mechanism of copper and its alloys in marine environment, Equip. Environ. Eng. 10 (21) (2024) 127–136, https://doi.org/10.7643/issn.1672-9242.2024.10.016.

[40] Y. Chen, Z. Li, H. Wang, Y. Wang, Y. Peng, L. Liu, Corrosion behavior of T2 copper in static artificial seawater, Mater. Prot. 2 (2018) 14–17, https://doi.org/10.16577/j.cnki.42-1215/tb.2018.02.004, 52.

[41] Y. Sun, C. He, J. Yang, Y. Ling, P. Chi, Research progress on corrosion and protection of copper alloys in seawater, Mater. China. 11 (2023) 874–883, https://doi.org/10.7502/j.issn.1674-3962.202111006.

[42] X. Yu, X. Zhang, S. Wang, G. Feng, A computational study on water adsorption on Cu2O(111) surfaces: the effects of coverage and oxygen defect, Appl. Surf. Sci. 343 (2015) 33–40, https://doi.org/10.1016/j.apsusc.2015.03.065.

[43] X. Yu, C. Zhao, T. Zhang, Z. Liu, Molecular and dissociative O2 adsorption on the Cu2O(111) surface, Phys. Chem. Chem. Phys. 31 (20) (2018) 20352–20362, https://doi.org/10.1039/C8CP03035A.